Journal of
Applied Remote Sensing

RemoteSensing.SPIEDigitalLibrary.org

Detection of Pb–Zn mineralization zones in west Kunlun using Landsat 8 and ASTER remote sensing data

Min Yang
Guangli Ren
Ling Han
Huan Yi
Ting Gao

SPIE.

Min Yang, Guangli Ren, Ling Han, Huan Yi, Ting Gao, "Detection of Pb–Zn mineralization zones in west Kunlun using Landsat 8 and ASTER remote sensing data," *J. Appl. Remote Sens.* **12**(2), 026018 (2018), doi: 10.1117/1.JRS.12.026018.

Detection of Pb–Zn mineralization zones in west Kunlun using Landsat 8 and ASTER remote sensing data

Min Yang,[a,b,*] Guangli Ren,[b] Ling Han,[a] Huan Yi,[b] and Ting Gao[b]
[a]Chang'an University, School of Earth Science and Resources, Key Laboratory for the Study of Focused Magmatism and Giant Ore Deposits, MLR, Xi'an, China
[b]Xi'an Centre of China Geological Survey, Xi'an, China

Abstract. The integration of Landsat 8 OLI and ASTER data is an efficient tool for interpreting lead–zinc mineralization in the Huoshaoyun Pb–Zn mining region located in the west Kunlun mountains at high altitude and very rugged terrain, where traditional geological work becomes limited and time-consuming. This task was accomplished by using band ratios (BRs), principal component analysis, and spectral matched filtering methods. It is concluded that some BR color composites and principal components of each imagery contain useful information for lithological mapping. SMF technique is useful for detecting lead–zinc mineralization zones, and the results could be verified by handheld portable X-ray fluorescence analysis. Therefore, the proposed methodology shows strong potential of Landsat 8 OLI and ASTER data in lithological mapping and lead–zinc mineralization zone extraction in carbonate stratum. [DOI: 10.1117/1.JRS.12.026018]

Keywords: lead–zinc ore; Landsat 8; ASTER; band ratios; principal component analysis; spectral matched filtering.

Paper 180034 received Jan. 12, 2018; accepted for publication Apr. 30, 2018; published online May 15, 2018.

1 Introduction

Remote sensing plays a pivotal role in many areas of the geosciences, geography, and environmental sciences. New generation, advanced remote sensing has been used in the past few decades in lithological mapping, mineral exploration, and environmental geology.[1–4] Due to the technical development of remote sensing,[5] many efficient image processing methods have been designed to map boundaries of intrusive bodies and hydrothermal zones, especially in inaccessible regions.[6] Landsat 8 is an Earth observation satellite, which was launched on February 4, 2013, and provides increased coverage of the Earth's surface. It is a free-flyer astro-vehicle equipped with two sensors, the operational land imager (OLI) and the thermal infrared sensor. The OLI imager collect images in seven bands, including visible, near-infrared (VNIR) and short-wave infrared (SWIR) bands. They are characterized by their high signal-to-noise radiometer performance, allowing 12-bit quantification of data for better land-cover discrimination. The spatial resolution of Landsat 8 is from 15 to 100 m on the Earth's surface.[7,8] The Advanced Space-borne Thermal Emission and Reflection Radiometer (ASTER), carrying the Terra platform (EOS), was launched in December 1999. It has lower signal-to-noise radiometer performance, allowing 8-bit quantification of data, but records solar radiation in 14 VNIR–SWIR–TIR bands.[9] Some remote sensing studies have been successfully processed, ASTER and Landsat 8 OLI data for lithological mapping[10] and for mineral detection to assist ore exploration.[11] In the VNIR (380 to 780 nm) and SWIR (900 to 2500 nm) regions, iron oxides,

*Address all correspondence to: Min Yang, E-mail: ymin@cgs.cn

carbonates, hydroxyl, and hydroxide minerals show molecular absorption features induced by their overtones and combination tones.[12] These minerals are some of the most common alteration products related to hydrothermal seeps.[13]

The study area is located on the west Kunlun metallogenic belt 700 km south to Delhi and 550 km northwest to Kashgar (Fig. 1). Although this inaccessible high altitude region is over 5000 m high, many geological studies indicate the high potential for lead–zinc deposit exploration using geochemical and aero geophysical methods. According to Zhang et al.,[14] the west Kunlun mountains, which are attracting international attention, is one of the largest prospective districts for exploring large- and super-large-scale lead–zinc ore deposits in central Asia.[15] Tectonically, this district is also an important section of the western Kunlun orogenic belt, being located between the Tethyan tectonic domain and the ancient Asian tectonic domain. Several huge ore-forming belts, such as the north Tibet ore-forming belt, Sanjiang ore-forming belt, and West Kunlun ore-forming belt, cross the west Kunlun mountains.[16] The ore-forming geological conditions, including stratum, structure, and magma activities, have revealed a favorable environment for mineralization, and a large number of metallic ores of different varieties have been found in the western part of the Kunlun orogenic zone.[17,18] These mineral deposits and mineralized zones, including seven sub-belts of mineralization and 18 mineralization sites, are regularly located along the metallogenic belts.[19] Huoshaoyun lead–zinc ore field, which

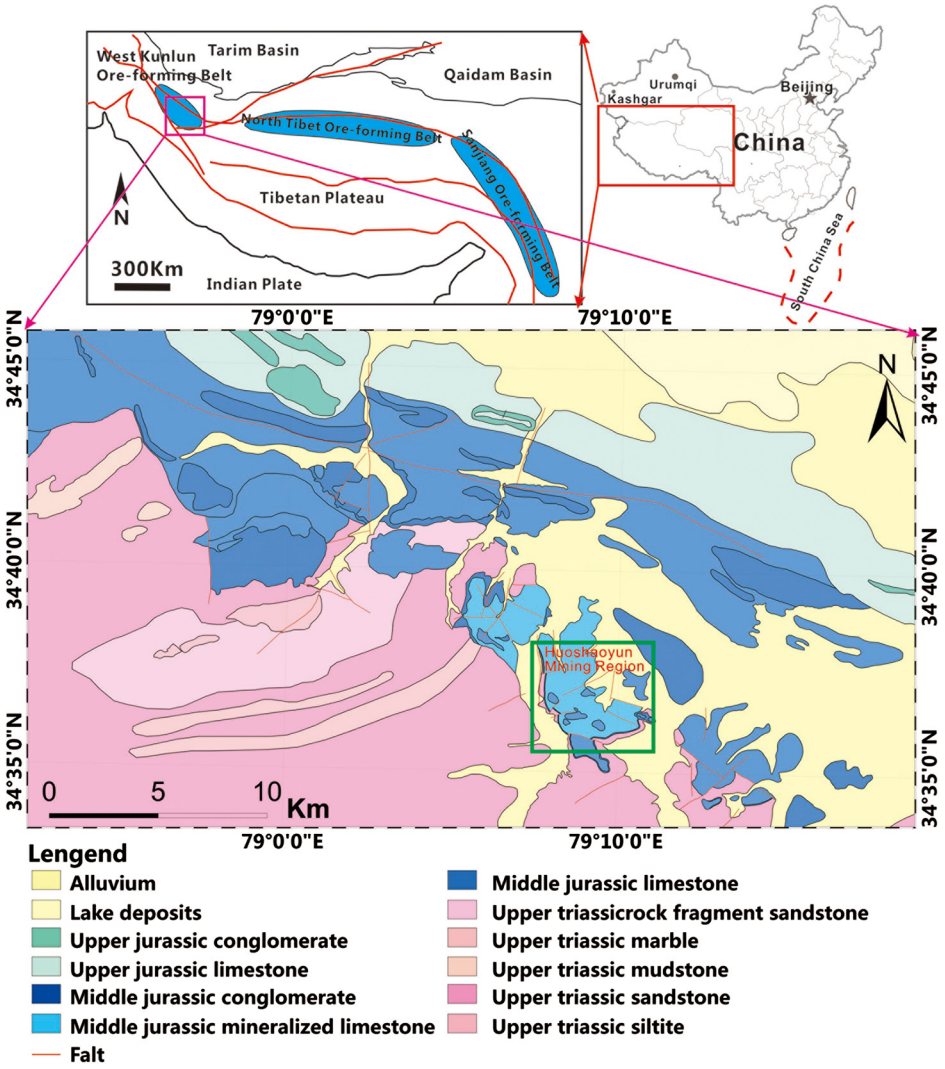

Fig. 1 A regional geological map showing the location of the study area.

was newly discovered in 2015, is bearing in Jurassic Longshan group, including a set of shallow marine carbonate rocks, clastic rocks, and locally interbedded volcanic and gypsum layers. The Longshan group is divided into two lithological sections: the first section is gray-brown and gray-purple thick-bedded glutenite; the second section is gray, dark gray, brown, and red thin- to thick-bedded limestone (Ls), locally imbedded gray-purple amygdaloidal basalt and dacite. Triassic mud-sandstone (Ms) is also present in the study area, and the stratigraphic contact relationship between the Triassic and middle Jurassic stratums is angular unconformity.

Some remote sensing studies have used shuttle imaging radar, TM, ETM^+, and ASTER data for volcano mapping, tectonic mapping, rupture zone detection, and metallogenic prognosis in the east part of Kunlun mountains. Some other studies have applied TM, ASTER, or even hyperion data successfully on gold prospecting in southwest Tianshan mountains.[20–26] But, in the west Kunlun mountains, only a limited number of research have used ETM^+ and WorldView-2 data in mapping alteration information by traditional processing methods, including false color composite and principal component analysis (PCA) in the west Kunlun ore-forming belt.[27,28] The authors of this research have accomplished a remotely sensed iron information extraction study in the west Kunlun area by processing WorldView-2 multispectral data with spectral matched filtering (SMF) method, one magnetite mineralization location had been discriminated successfully. Since the spectral resolution limitations of the WorldView-2 data (lack of SWIR bands), no detailed information of carbonate and hydroxyl bearing minerals could be obtained in the previous research.[29]

The main objective of this task is to first apply ASTER and Landsat 8 OLI data processed by a series of image mapping methods for the discrimination of lithological units and lead–zinc bearing mineralization detection in the periphery of the Huoshaoyun ore field. The Huoshaoyun area lacks a remote sensing study and is very suitable for remote sensing exploration due to the SWIR active carbonate minerals.

2 Materials and Methods

2.1 *Data*

A cloud-free level 1T Landsat 8 OLI image was obtained on August 1, 2013. The image projection is Universal Transverse Mercator zone 44N from WGS-84 datum. The radiance was calculated and the image was subjected to atmospheric correction using the fast line-of-sight atmospheric analysis of spectral hypercube module (FLAASH). The ASTER level 1B data used in this study was acquired on October 17, 2003. The images have been pregeoreferenced to UTM zone 44 north projections with WGS-84 datum. The VNIR bands were resampled to 30 m, and the nine bands VNIR to SWIR data were also corrected for atmospheric effects using the FLAASH module. The difference of the acquired time of the two datasets does not pose challenges because this is a remote area largely unmodified over 10 years and the geological characteristics given by the focused studies are unchanged over that time period. We do, however, apply a unique atmospheric correction (FLAASH)to each dataset. The spectral curves of different rocks in this research for lithological mapping and accuracy evaluation were collected on both Landsat 8 OLI and ASTER data according to the pre-existing geological map and laboratory spectra.

2.2 *Band Ratios*

Band ratios (BRs) and red–green–blue (RGB) color composite (CC) were created with both Landsat 8 OLI and ASTER bands, on basis of laboratory spectra of the hydrothermal minerals and lithological units.[30–32] BR is a technique in which the digital number value of one band is divided by another band based on absorption characteristics, in order to highlight certain lithological units that cannot be easily distinguished by the raw imagery. Different color combination images (CCs) were used to enhance lithological units and hydrothermally altered mineralization zones at the regional scale.

2.3 *Principal Component Analysis*

PCA is a statistical tool for producing uncorrelated bands by finding a set of orthogonal axes that have their origin at the data mean and that are rotated so the data variance is maximized.[6] The PCA technique is traditionally used to compress a large correlated band into smaller uncorrelated bands named principal components (PCs).[10] This process eliminates the data redundancy, isolates the noise in the output PC bands, and therefore enhances certain types of spectral signatures from the background. The PCA algorithm and its eigenvector matrices were applied to the proposed Landsat 8 OLI and ASTER VNIR-SWIR bands for emphasizing the distribution of the different rock units and mineralization zones in the study area.

2.4 *Spectral Matched Filtering*

SMF is a smart tool for extracting certain materials based on spectral reflectance data-matching with the images. It strengthens the signals of the desired targets and minimizes the signals of the background.[33] The results of the SMF appear as a gray-scale image and show values between 0 and 1, where 0 represents a mismatch to the targets and 1 represents a complete match. Then, thresholds can be set to create segmentation maps to show areas with good matches to the targets. Unlike linear unmixing, SMF does not require knowledge of all the attributes within the scene. Thus, in pixels of highly mixed lithologies, where identification of all the attributes is difficult, SMF may be an efficient tool for the identification of certain minerals, such as carbonate minerals, iron oxide minerals, and OH-bearing minerals.[34]

SMF is frequently used to determine the abundances of the defined target using a partial unmixing:

$$\mathrm{SMF}(x) = (t-m)^T S^{-1}(x-m), \tag{1}$$

where t, m, S, and x are target vector, background mean, background covariance, and sample vector, respectively.

2.5 *Field Work*

The carbonate minerals with abundant gypsum parts in the mineralization zones are considered to be the main target for lead–zinc exploration.[35] Considering that the spectra from the spectral library cannot be representative, spectra of the well-known targets were collected as preparation for identifying the mineralization zones in the Ls rock unit. For this purpose, both Landsat 8 OLI and ASTER VNIR-SWIR bands were used to resample spectral curves from target areas that were used to distinguish the mineralized limestone (MI) from unmineralized Ls.

Some typical lithological samples of the wide range of lithologies in the study area were collected as criterion materials in the mapping and discrimination of the different rocks. In addition, some samples collected in the Huoshaoyun ore field were also sampled for spectral, chemical, and mineralogical research. Moreover, *in situ* XRF measurement was also performed after the selection of verification areas, in order to trace the location of the high potential ore-bearing zones. The *in-situ* XRF measurement on rock surface is conducted using handheld portable XRF instrument (Skyray Genius 7000) manufactured by Skyray® Ltd., Suzhou, China. The instrument contains a battery operated miniature X-ray source (W anode) and no radioisotopes, and the relative contents of elements (wt. %) could automatically calculated using the Skyray "rock mode" software without any sample preprocessing.

2.6 *Laboratory Work*

Powder X-ray diffraction (XRD) analysis, without any chemical pre-treatment, was used to measure the mineral compositions of the samples collected in the ore body and wall rock. The differences of mineral composition between ore rocks and wall rocks are very helpful in determining the SWIR spectral features of mineralization zones. Traditional XRD was conducted on a new $D/$ max 2500, Rigaku diffract meter connected with a graphite monochromator, and working at 35 kV and 50 mA using Cu-Kα radiation at the Key Laboratory for Magmatism and Giant Ore Deposits, Ministry of Land and Resources, China. A portion of the samples were

further smashed to fine powder (300 item) using a small, clean mortar, and then mounted on a plastic holder (φ, 25 mm; depth, 1 mm) for XRD measurement. The oriented samples were scanned over an interval of 0.020 deg (1.2 s) at a scanning speed of 1.000 deg / min. Entrance, scattering, and receiving slits were 2 deg, 1 deg, and 0.30 mm, respectively.

All SWIR spectra were obtained using a PANalytical ASD FieldSpec Pro® 3 spectrometer (hereafter referred as ASD) that records spectra from the 350 to 2500 nm wavelength region with a spectral resolution of 10 nm and a sampling interval of 1 nm in the SWIR (1300 to 2500 nm) region. The spectrometer was connected to a contact probe with an internal halogen bulb, which ensures stable illumination conditions during data collection. All the spectra were subset from 1300 to 2500 nm for spectral analysis, because most of the key features occur in this region.

The lithological mapping accuracy was quantitatively evaluated by test samples using confusion matrixes and kappa coefficient. The overall accuracy is the ratio between all correct classified pixels and the total pixels error classified. The kappa coefficient is a statistical measures inter-rater agreement for qualitative (categorical) items. The test samples were selected randomly according to the pre-existing geological map.

3 Results

3.1 *Mineralogical Compositions and Spectral Characteristics*

Six samples collected from surrounding rocks and different parts of the Huoshaoyun ore body are illustrated in Table 1. The mineral constituents of the samples calculated from the XRD data in this study were simple, with up to five or six kinds of minerals in each sample. However, there are some mineral differences between the ore body and their wall rocks, not only in the composition, but also in their relative contents. The ore body samples HSY-04, HSY-12b, and HSY-12a were dominated by cerussite and smithsonite with relatively abundant gypsum (4% and 5%), whereas the surrounding rock samples HSY-03, HSY-06, and HSY-13 were dominated by calcite, dolomite, and relatively poor gypsum (1%).

These distinctions in the mineral constituents between the ores and their surrounding rocks may be shown by field spectral data measured by ASD instrument, or even remote sensing data. As shown in Fig. 2, three absorption features were shown. The deeper absorption peaks that occur at around 2340 and 2450 nm (ASTER band 8 and 9) are due to carbonate minerals, whereas the weak absorption peaks that appear at around 2210 nm (ASTER band 6) are related to gypsum. These features may make the identification of mineralization zones from unmineralized Ls and other rock units easier when using remote sensing data.

3.2 *Band Ratios*

As used in the ratios, the bands in both Landsat 8 OLI and ASTER images were selected according to the absorption features of the different lithologies (Fig. 3). The ratios, OLI 5/4 and ASTER 3/2, were calculated for discriminating alluvium (Al), due to its intense absorption in band 4 of

Table 1 Mineral composition (wt. %) of the mineralization zones.[a]

		Smithsonite	Cerussite	Calcite	Dolomite	Gypsum	Quartz	Illite	Kaolinite
From ore bodies	HSY-04	26	65			5	4		
	HSY-12b	6	90			4			
	HSY-12a	55	40		1	4			
From surrounding rocks	HSY-03	1		70	24	1	4		
	HSY-06a	1	1	95			1		
	HSY-13	2	2	90		1	4	1	

[a]The mineral components were calculated using XRD data.

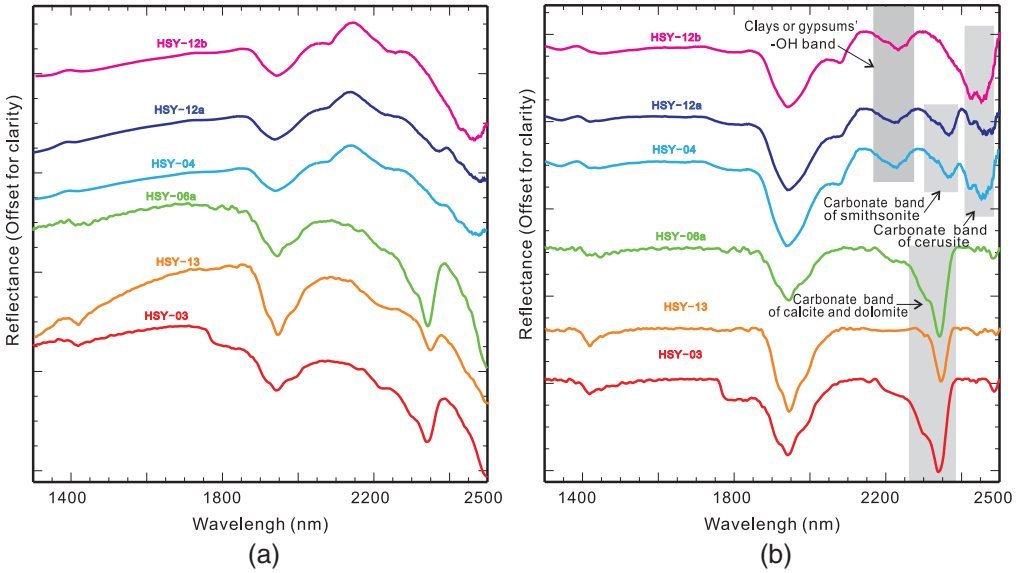

Fig. 2 Laboratory SWIR reflectance spectra collected by (a) ASD instrument and (b) continuum removal spectra of samples collected from surrounding rocks and mineralization zones.

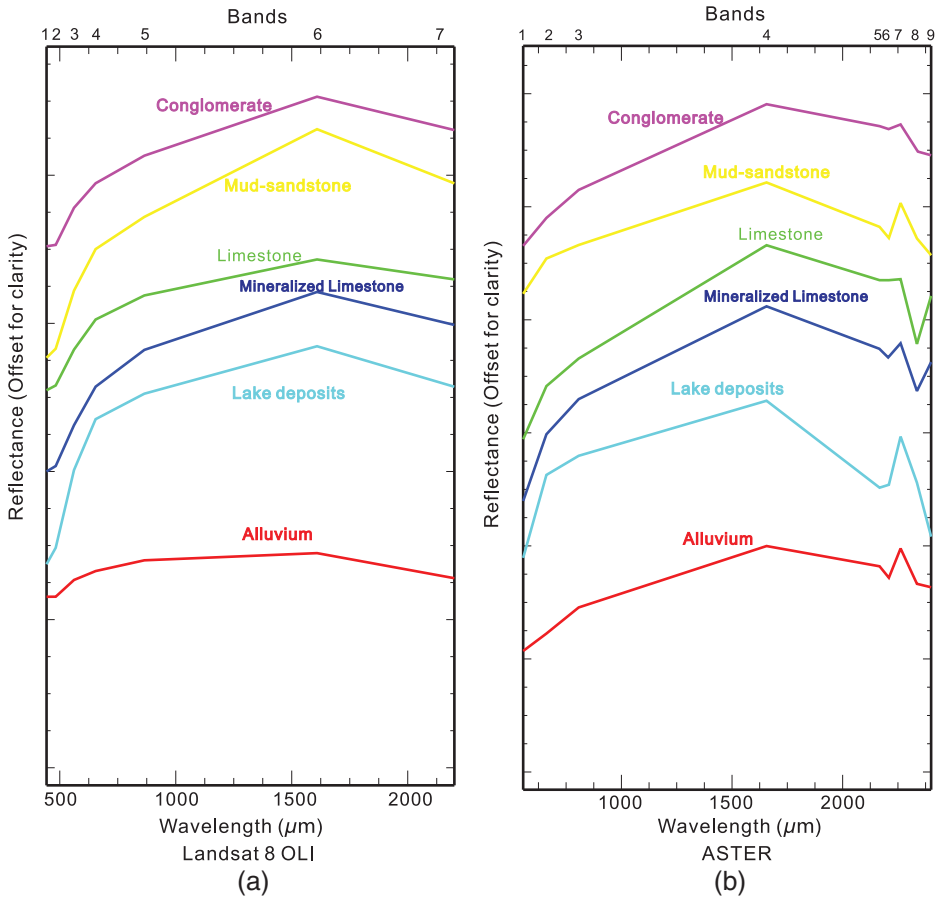

Fig. 3 Spectral curves of lithologies sampled from (a) OLI and (b) ASTER images.

OLI and band 2 of ASTER at 650 and 660 nm (red band), probably related to the iron oxides in the sediments.[36–38] The Ms, which is rich in mica and clay minerals, is lightened by the ratios OLI 6/5 and ASTER 5/3, for its spectra, exhibits high reflectance at band 6 of OLI and band 5 of ASTER, and shows an absorption at 860 nm (band 5 of OLI) and 800 nm (band 3 of ASTER),

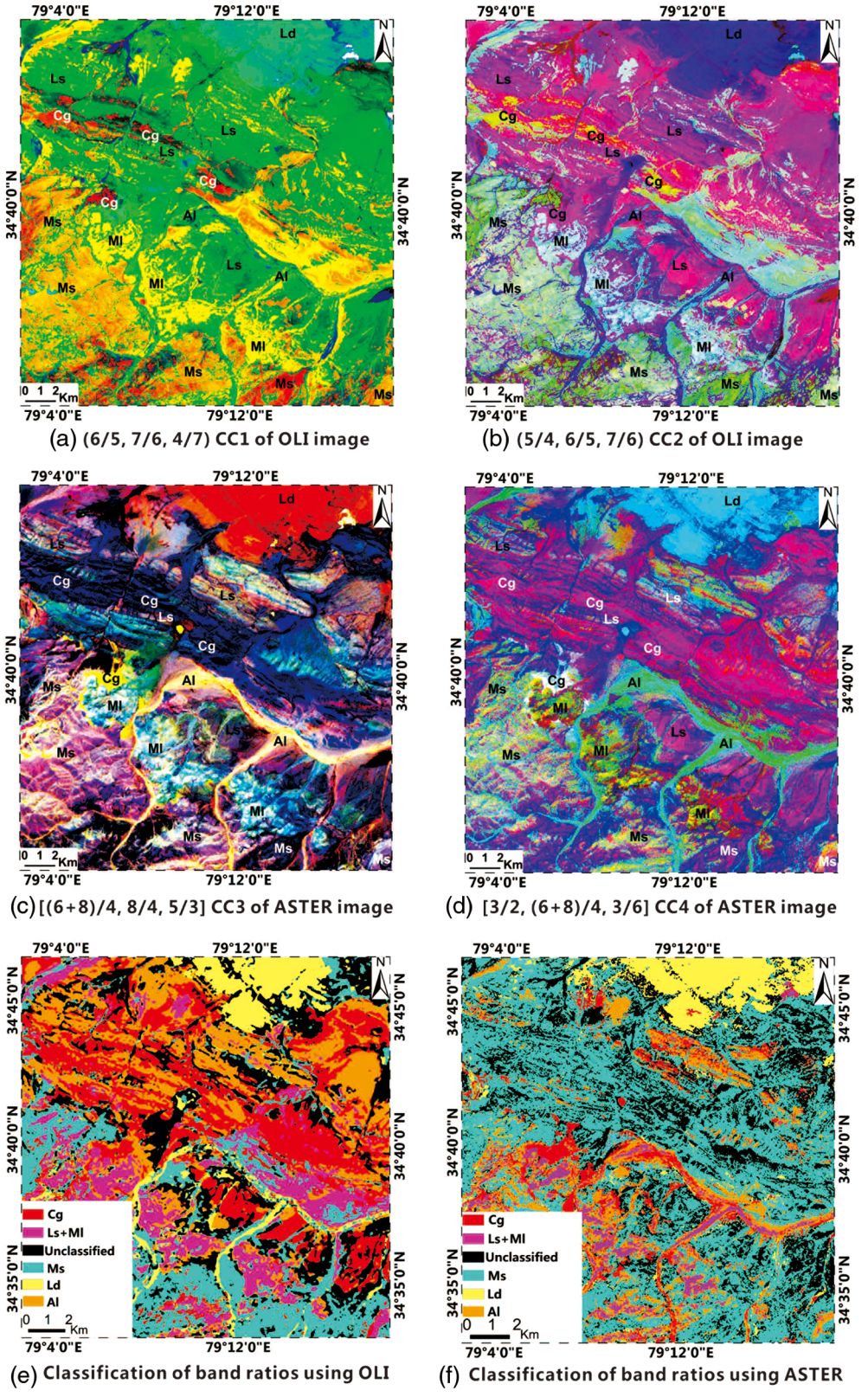

Fig. 4 BRs RGB CCs of both OLI and ASTER images. (a) 6/5,7/6,4/7 CC1 of OLI image, (b) 5/4,6/5,7/6 CC2 of OLI image, (c) $(6+8)/4$, 8/4, 5/3 CC3 of ASTER image, (d) 3/2, $(6+8)/4$, 3/6 CC4 of ASTER image, (e) classification of BRs using OLI, and (f) classification of BRs using ASTER.

corresponding to the NIR region. This absorption is also possibly due to the existence of iron oxides.[39–41] Compared with other spectra, an intense absorption of Al-OH group at band 7 of OLI and band 6 of ASTER near 2200 nm and a high reflectance in band 4 of OLI and band 3 of ASTER occur in conglomerate (Cg), which is due to mica or clay minerals.[9,40,42] Therefore, the ratios OLI 4/7 and ASTER 3/6 are used to distinguish this stratum. The Ls is highlighted by the ASTER ratio of 8/4 since its spectra show deep absorption in band 8, whereas this band is not available on OLI sensor. In addition, Ml spectra show high reflectance at band 6 of OLI and band 4 of ASTER, and show a weak absorption at band 7 of OLI and band 6 of ASTER near 2200 nm, potentially due to the weak gypsum and clay alteration.[37,43] The spectral curves sampled from the ASTER data, which show a deep absorption at band 8 (2330 nm), can be attributed to the carbonate minerals.[12,41] Consequently, the ratios $[[(6+8)]/4]$ of ASTER and (7/6) of OLI could be used to extract the Ml.

Two RGB color combination schemes for each sensor were selected to better extract the existing lithological units and mineralization zones on the basis of examining different combinations of ratios.[9,44–46] In CC1 (R6/5, G7/6, B4/7) of OLI, the Ms is represented by a yellow-orange color, which appears as purple in CC3 [R(6 + 8)/4; G8/4; B5/3] of ASTER and as light blue-green in CC2 (R5/4, G6/5, B7/2) of OLI. The Ml is distinguished by a light blue-white color in CC3 while it displays as light yellow in CC1. Alluvium (Al) and lake deposits (Ld) appear dark blue in CC2 (R5/4, G6/5, B7/6) of OLI, whereas they appear light blue to light green in CC4 [R3/2, G(6 + 8)/4, B3/6] of ASTER. Regarding Ls, it is characterized by green in CC1 and by pink-magenta in CC4. Additionally, Cg is marked by the dark blue color on CC3 and by the green-yellow on CC2 [Figs. 4(a)–4(d)]. Then, lithological maps were mapped according to the CCs RGB images of the two sensors, and five lithological units were classified [Figs. 4(e) and 4(f)] based on classification tools in ENVI 5.0 and pre-existing geological maps.

3.3 *Principal Component Analysis*

The results calculated from the PCA, which include PC bands, eigenvectors, and eigenvalues, are shown based on the covariance matrix in Tables 2 and 3.[36,41] PC1 contains the highest values (usually the total albedo of the scene) in both OLI and ASTER images (82.97% in OLI and 97.55% in ASTER). PC2 enhances the discrepancies between the VNIR bands (OLI bands 2, 3, 4, 5 and ASTER bands 1, 2, 3) and SWIR bands (OLI bands 6, 7 and ASTER bands 4, 5, 6, 7, 8, 9) by opposite signs.[42] In the remaining PCs, the signs and magnitude of eigenvectors could be analyzed in the discrimination of different objects.[47] The target objects are characterized by bright pixels if the eigenvector values are positive in the reflectance bands and negative in the absorption bands.[42] On the other hand, the importance of the output spectral band in that PC is described by its magnitude. A larger value represents more significance.[47] On the basis of examining the eigenvectors in the OLI PC matrix, the argillaceous and micaceous Ms can be mapped by high lightened pixels in PC3, due to its strong reflection at band 6 with a positive contribution (0.076) and absorption at band 5 with a prominent negative value (−0.686) [Fig. 5(a)]. The Ld could be marked by white pixels in PC4, owing to its positive value in band 6

Table 2 The matrix of eigenvectors calculated from the PCA on OLI image.

Eigenvector	Band 1	Band 2	Band 3	Band 4	Band 5	Band 6	Band 7	Eigenvalue (%)
PC 1	−0.257	−0.268	−0.353	−0.417	−0.459	−0.452	−0.386	82.97
PC 2	−0.412	−0.384	−0.319	−0.224	−0.038	0.555	0.470	16.63
PC 3	0.379	0.337	0.127	−0.273	−0.686	0.076	0.419	0.25
PC 4	0.372	0.238	−0.268	−0.594	0.331	0.375	−0.360	0.07
PC 5	0.171	0.043	−0.346	−0.194	0.410	−0.570	0.564	0.05
PC 6	0.389	−0.062	−0.695	0.549	−0.198	0.123	−0.082	0.02
PC 7	0.549	−0.778	0.288	−0.100	0.019	−0.012	0.009	0.00

Table 3 The matrix of eigenvectors calculated from the PCA on ASTER image.

Eigenvector	Band 1	Band 2	Band 3	Band 4	Band 5	Band 6	Band 7	Band 8	Band 9	Eigenvalues (%)
PC 1	−0.244	−0.300	−0.333	−0.416	−0.350	−0.345	−0.359	−0.309	−0.317	97.55
PC 2	0.554	0.506	0.417	−0.223	−0.167	−0.109	−0.264	−0.209	−0.245	1.72
PC 3	0.187	0.066	−0.106	−0.271	−0.372	−0.464	0.480	0.527	0.117	0.38
PC 4	0.277	−0.074	−0.287	−0.701	0.350	0.458	0.062	0.077	0.049	0.12
PC 5	0.606	−0.080	−0.605	0.407	0.103	−0.188	−0.204	−0.040	0.074	0.08
PC 6	0.100	−0.027	−0.125	0.140	−0.039	0.137	0.659	−0.357	−0.610	0.06
PC 7	0.051	−0.013	0.050	−0.135	0.009	−0.211	0.298	−0.667	0.632	0.04
PC 8	−0.087	0.013	0.115	−0.096	0.759	−0.587	0.041	0.031	−0.216	0.03
PC 9	0.366	−0.798	0.474	0.013	−0.035	−0.012	−0.004	0.048	−0.032	0.01

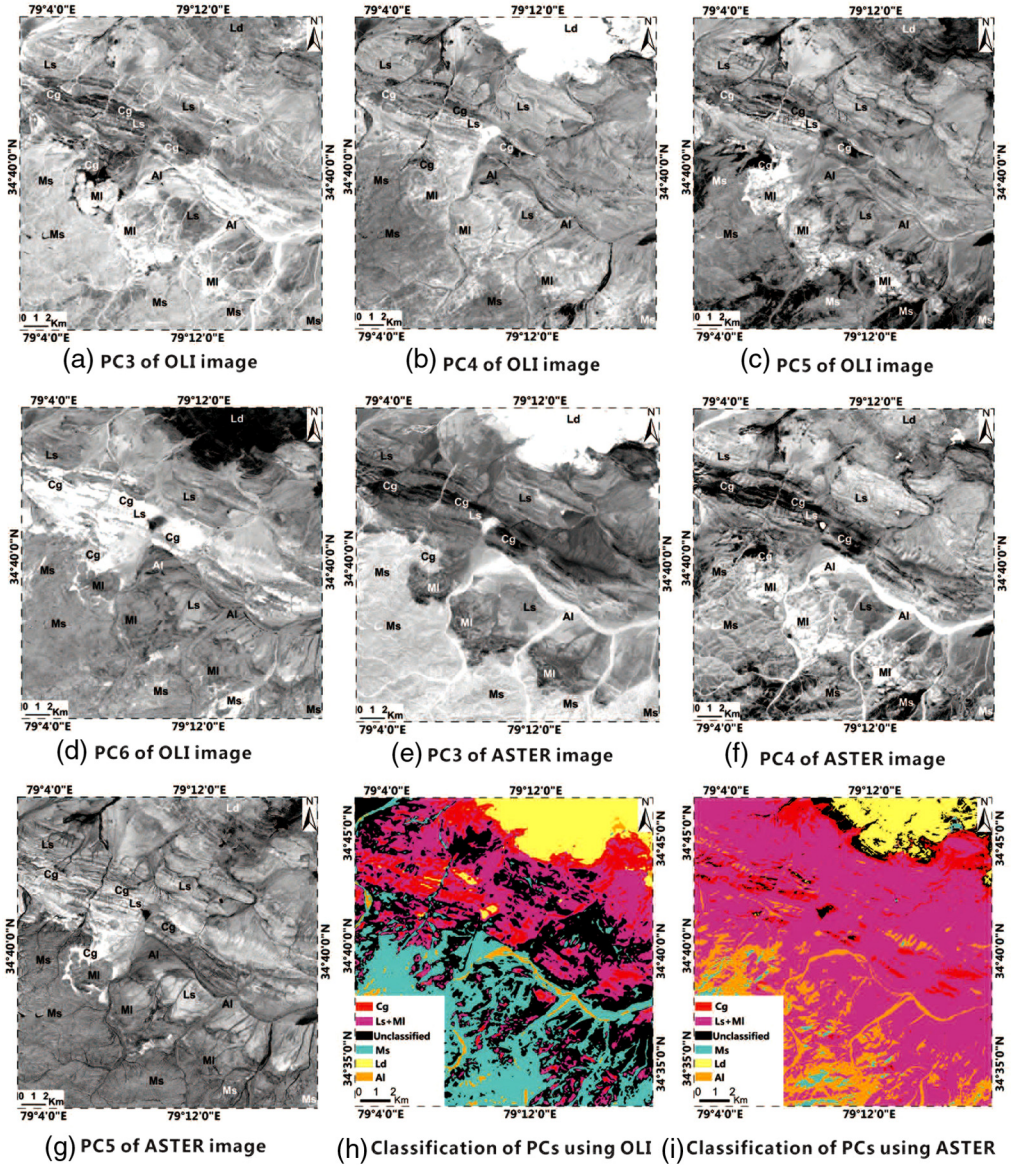

Fig. 5 PCA of both OLI and ASTER images. (a) PC3 of OLI image, (b) PC4 of OLI image, (c) PC5 of OLI image, (d) PC6 of OLI image, (e) PC3 of ASTER image, (f) PC4 of ASTER image, (g) PC5 of ASTER image, (h) classification of PCs using OLI, and (i) classification of PCs using ASTER.

(0.375) and negative value in band 7 (−0.360) [Fig. 5(b)]. Ml could be highlighted in PC5 due to its absorption feature in band 4 (−0.194) and intense reflectance in band 7 (0.564) [Fig. 5(c)]. Cg is mapped by highlighted pixels in PC6, presenting the absorption feature in band 5 (−0.198) and reflectance feature in band 4 (0.549) [Fig. 5(d)].

Regarding the ASTER PC matrix, the clayceous and micaceous Ld could be highlighted in PC3 using its positive and negative values in band 8 (0.527) and band 4 (−0.271), respectively [Fig. 5(e)]. Still in this PC, the Ms could be represented by gray pixels because of the positive contribution of band 7 (0.480) and negative contributions of band 6 (−0.464) and band 5 (−0.372). Cg is marked by bright pixels in PC5 with its negative and positive values in band 3 (−0.605) and band 4 (0.407), respectively. Also, in this PC, Ls with calcite and dolomite could be marked by gray pixels because of the positive value of band 1 (0.606) and negative value of band 7 (−0.204) [Fig. 5(g)]. Finally, Ml is shown by bright pixels in PC4, owing to the positive contribution of band 6 (0.458). In the same PC, bright pixels show Al, attributed to the weak positive contribution in band 7 (0.062), which represents the absorption feature of this lithology[9,42,44,48] [Fig. 5(f)]. The other remaining PCs, for both sensors, mainly contain noise, and therefore cannot provide any information. Furthermore, two lithological maps were also mapped according to the PCA images and pre-existing geological maps [Figs. 5(h) and 5(i)].

3.4 *Spectral Matched Filtering*

For discriminating mineralization zones and other lithological units, the SMF technique was also used for both OLI and ASTER images. Because the ASTER data have more bands in SWIR than Landsat 8 OLI data, it can show more detail in spectral features. In this case, the ASTER data is more efficient to use for the SMF method for the identification of the mineralization Ls unit. The results of this method, which are shown in Figs. 6(a) and 7(b), indicated that the six kinds of lithological units, including Ld, Ls, Ms, Cg, Al, and mineralization limestone (Ml), can be well matched. Thus, spectral curves of the different rocks were selected from both OLI and ASTER images and verified by field work and laboratory spectral collection.

As shown in the mapping results based on SMF using Landsat 8 OLI 7 bands data and ASTER 9 bands data, the ASTER data generally produced a better separation of lithological units [Fig. 6(b)]. On the other hand, the Landsat 8 OLI could also exactly separate Ls and/or MI from other types of rocks, but it fails to distinguish Al from Ms [Fig. 6(a)].

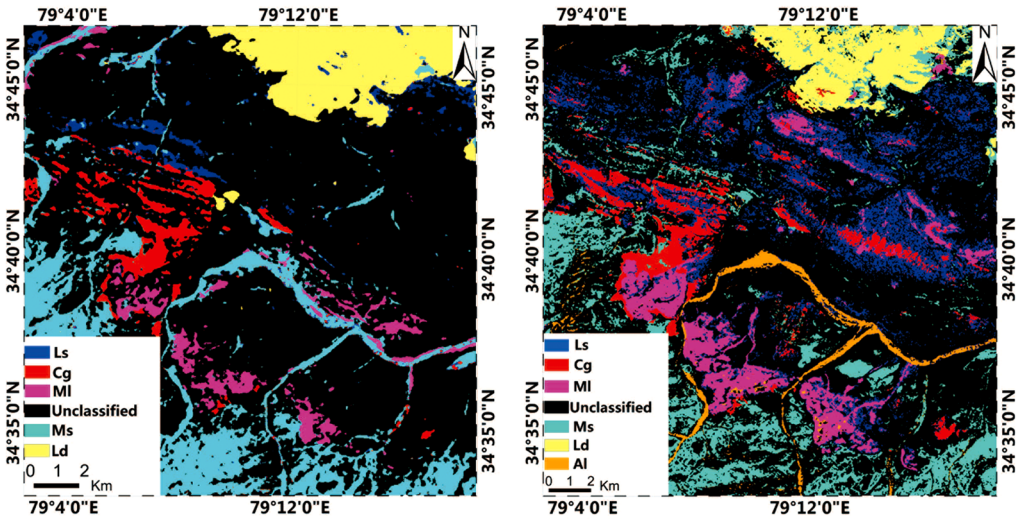

Fig. 6 Results of SMF to distinguish MI using (a) OLI and (b) ASTER.

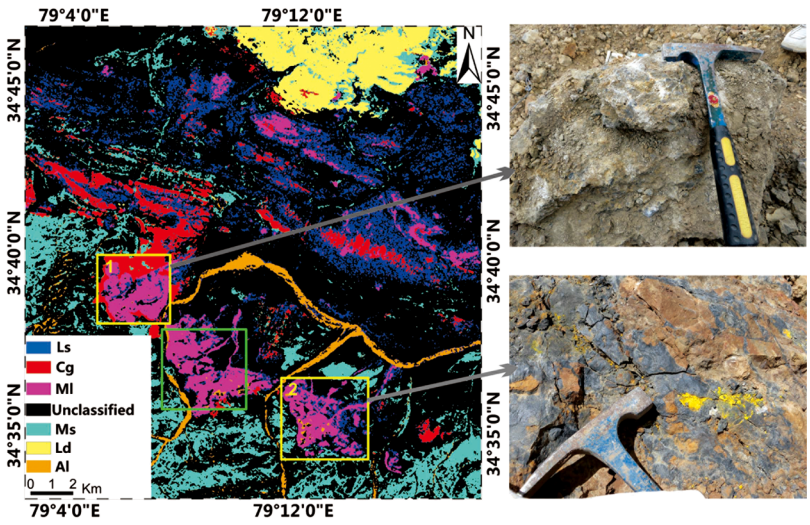

Fig. 7 Distribution of lead–zinc prospects (magenta pixels represent MI, the yellow blocks with numbers represent prospects, and the green block represents the Huoshaoyun ore field).

4 Discussion

In this section, the accuracies of the two kinds of data using the three different methods are discussed, then the mapping results are integrated with *in situ* XRF measurements for lead–zinc verification.

4.1 *Accuracies of the Methods*

To examine the mapping accuracies of the two kinds of data in using the three methods above, the confusion matrixes were also calculated by comparing, pixel by pixel, the result of lithological mapping, and the geological map. ROIs covering different lithological units were selected according to the pre-existing geological map. The review of the confusion matrix is shown in Tables 4–9. The overall accuracies and the kappa coefficients of the ASTER data in using the three methods are as follows: SMF 83.13%, 0.76; PCA 80.46%, 0.73; BRs 62.98%, 0.52. The overall accuracies and the kappa coefficients of the OLI data in using the three methods are as follows: SMF 62.98%, 0.52; PCA 53.70%, 0.34; and BRs 47.33%, 0.23. The comparison between the diagonals of confusion matrixes shows that the ASTER data produce better results than OLI sensor, especially using the SMF method. The comparison between the three methods indicates that the SMF method had the best accuracy in lithological mapping and the BRs method had the poorest accuracy. In addition, the result of the ASTER data using the SMF method discriminated six kinds of lithological units, whereas other results

Table 4 The confusion matrix of the OLI image of the BRs method.

Class	Ls+Ml	Ld	Cg	Al	Ms
Ls+Ml	66.51	2.94	40.08	3.22	67.11
Ld	3.48	97.03	1.28	5.13	17.36
Cg	11.90	0.03	51.81	38.00	3.99
Al	13.29	0.00	6.67	50.46	6.00
Ms	4.81	0.00	0.16	3.19	5.53
Total	100	100	100	100	100

Note: Overall accuracy: 47.33%; kappa coefficient: 0.23.

Table 5 The confusion matrix of the OLI image of the PCA method.

Class	Ld	Cg	Ms	Al	Ls+Ml
Ld	69.35	0.00	0.00	0.05	0.00
Cr	0.14	3.40	5.02	5.85	4.85
Ms	30.43	28.87	61.09	84.68	42.93
Al	0.08	25.90	13.43	0.18	2.50
Ls+Ml	0.00	41.84	20.46	9.24	49.72
Total	100	100	100	100	100

Note: Overall accuracy: 53.70%; kappa coefficient: 0.34.

Table 6 The confusion matrix of the OLI image of the SMF method.

Class	Ms	Ld	Cg	Ls	Ml
Ms	46.49	15.27	7.66	4.02	13.42
Ld	8.74	81.88	8.03	1.50	3.59
Cr	3.34	1.65	61.55	17.19	0.43
Ls	13.05	1.17	22.56	65.49	8.86
Ml	28.38	0.02	0.20	11.80	73.69
Total	100	100	100	100	100

Note: Overall accuracy: 62.98%; kappa coefficient: 0.52.

Table 7 The confusion matrix of the ASTER image of the BRs method.

Class	Ld	Ms	Cg	Ls+Ml	Al
Ld	99.98	12.54	0.64	0.81	0.28
Ms	0.00	34.59	32.89	9.54	64.33
Cg	0.00	1.68	2.29	0.97	12.78
Ls+Ml	0.00	45.71	59.80	80.15	22.50
Al	0.01	5.47	4.37	8.54	0.10
Total	100	100	100	100	100

Note: Overall accuracy: 62.98%; kappa coefficient: 0.52.

Table 8 The confusion matrix of the ASTER image of the PCA method.

Class	Cg	Ms	Ld	Al	Ls+Ml
Cg	5.11	0.08	1.17	0.01	12.07
Ms	63.02	93.94	0.28	60.39	4.06
Ld	1.91	0.25	96.27	0.38	6.10
Al	11.92	4.98	1.37	39.12	0.01
Ls+Ml	18.05	0.74	0.92	0.10	77.77
Total	100	100	100	100	100

Note: Overall accuracy: 80.46%; kappa coefficient: 0.73.

Table 9 The confusion matrix of the ASTER image of the SMF method.

Class	Al	Ld	Ms	Cg	Ls	Ml
Al	83.22	0.12	2.09	0.10	0.19	0.12
Ld	6.36	99.06	0.20	32.54	5.43	3.09
Ms	2.31	0.20	78.12	1.72	3.32	1.58
Cg	7.90	0.28	6.54	20.32	15.23	6.54
Ls	0.10	0.18	11.87	28.89	50.50	9.02
Ml	0.11	0.16	1.18	16.42	25.32	79.65
Total	100	100	100	100	100	100

Note: Overall accuracy: 83.13%; kappa coefficient: 0.76.

showed five kinds of lithological units. Al was missed in the OLI data using the SMF method, and the two kinds of data using the BR and PCA methods failed to discriminate Ml from Ls.

The good accuracies of the classification results of the Ld, ranging from 69.35% to 99.98%, are due to their strong absorption feature in band 1 of OLI and band 5 of ASTER. The satisfactory accuracies of the Ml and/or Ls are between 49.72% and 80.15%, and these results are important to lead–zinc exploration. According to the confusion matrixes, Cg and Al have high values of misclassifications. These values have influenced the overall accuracies because these lithological units are unconsolidated sediment that consists of a mixture of products resulting from the accumulation of surrounding rocks.

4.2 *Application to Pb–Zn Exploration*

According to the mapping results and the existing geological map, two verification areas were recognized and selected for *in situ* XRF measurement and field work. These areas are indicated by numbers in Fig. 7. The mineral component contents of each area were measured using a Skyray Genius 7000XRF instrument. The whole of the two areas were verified, and abundant lead and zinc components were found, rather than Ls units, in the periphery of the ore body. The first area showed lead and zinc content ranging from 0.7443% to 26.2601%, and from 0.157% to 62.8469%, respectively, and was found in Ls units, where gypsum alteration is well developed. The second area was also found in Ls units affected by gypsum alteration and featured lead and zinc components ranging from 0.5283% to 59.8364%, and from 2.9808% to 68.2128%, respectively (Table 10). They are all found in Ls formations as they are in the Huoshaoyun mining area. The two discovered high potential areas suggest that Landsat 8 OLI and ASTER images are valuable for lead–zinc exploration in Ls rocks.

Although two potential ore-bearing areas were recognized, a large area was unclassified on the lithological maps, especially using the SMF method. This discrepancy can be ascribed to the pervasive diluvium mixing with a variety of lithological debris, mainly including Ls, Ms, and Cg. In this case, the exact lithology of these mixtures was difficult to identify using the SMF method.

Since Landsat 8 OLI and ASTER images are freely available and easy to download and process, a three-step procedure was developed for lead–zinc exploration in Ls stratums. The Landsat 8 OLI images, BR, and PCA methods are used in the first step to map the different lithological units, especially to discriminate the Ls from other rock units. In the second step, ASTER data and the SMF method are used to discriminate mineralization zones from Ls, and then the possible lead–zinc enriched areas are selected. In the last step, these areas are further evaluated by field survey and *in situ* XRF measurements to find areas of high potential for ore exploration.

The Landsat 8 OLI and ASTER data processed by a series of techniques, including BRs, principle component analysis, and SMF, were applied to map the lithological distribution and mineralization zones based on the knowledge of found Huoshaoyun Pb–Zn ore in the study area.

Table 10 *In situ* XRF measurement of the two verification areas.

Area 1			Area 2		
Measurement No.	Pb (wt. %)	Zn (wt. %)	Measurement No.	Pb (wt. %)	Zn (wt. %)
HSY16-07	1.0254	38.2727	HSY16-35	1.0199	63.5949
HSY16-08	2.1339	0.157	HSY16-36	0.8048	68.2128
HSY16-10	7.128	3.7247	HSY16-37	9.1603	36.8737
HSY16-14	4.197	3.9666	HSY16-38	3.1489	46.6946
HSY16-25	0.7443	60.179	HSY16-39	28.7427	28.9527
HSY16-26	0.8596	62.8469	HSY16-40	5.4181	67.68
HSY16-27	18.7559	39.4437	HSY16-41	59.8364	2.9808
HSY16-28	6.9946	32.3956	HSY16-42	4.8499	35.0357
HSY16-30	1.0355	59.992	HSY16-47	48.7373	3.0388
HSY16-31	26.2601	26.3382	HSY16-48	22.5788	26.1557
HSY16-34	5.3624	63.2095	HSY16-49	0.5283	54.9781

By examining the results calculated from the three kinds of methods, ASTER data perform better classification accuracies than Landsat 8 OLI under the same method. This advantage should be contributed by the band richness in SWIR region of ASTER imagery.[46] But the results of Landsat 8 OLI imagery processed by the three methods still reached satisfactory classification accuracies in regional scale mapping.[10,49] The classification accuracies of SMF in processing the same data are generally better than BR and PCA on basis of a reliable field work and representative sampling.[50] Since the accuracies relatively lower than SMF, the lithological discrimination based on BR and PCA may still very be useful in some inaccessible, alpine areas lack of geological data on Kunlun mountains and Tibetan plateau. Additionally, some research have reported some Pb–Zn ores in the west Kunlun area as Mississippi valley type (MVT) deposit, and the abundant cerusite, smithsonite, and gypsum recognized in the Huoshaoyun mineralization zones may indicate a sulphide desulphurization after galena and sphalerite deposited.[51,52] So, we describe the Huoshaoyun Pb–Zn ore as the MVT secondary oxidation type (SOT). This finding would help exploration geologists to trace the potential extension of Huoshaoyun Pb–Zn ore body and analyzes the ore bearing conditions.

Because of the low spatial resolution of ASTER and Landsat 8 OLI VNIR-SWIR data (30 m/pixel), it is hard to further discriminate the thin mineralization zones with its width less than 30 m in detail. The recently launched WorldView-3 satellite of Digital Globe has provided new opportunities supporting large scale geological mapping in both VNIR and SWIR bands, after the regional scale mapping by ASTER and OLI data.[53–56] Therefore, ASTER, OLI data, and WorldView-3 data are possibly integrated using the similar procedures in further research aiming at more practical and accurate methodology of locating unknown mineralization zones in abominable area.

5 Conclusions

The application of the Landsat 8 OLI and ASTER data for mapping lithological units and Pb–Zn mineralization zones in the Huoshaoyun area demonstrates that the two kinds of data could provide reliable distribution of lithologies and mineralization zones. Findings of our work are as follows:

1. The image processing techniques, including BRs, PCA, and SMF, were utilized to process the two kinds of data for mapping the distribution of different rocks and for

detecting the potential mineralization zones based on the image spectra of the known lithologies and deposits. The mapping accuracies of the MI discriminated by the two kinds of data and the three methods were between 49.72% and 80.15%. The result of ASTER data processed by matched filtering method reaches the best accuracy in mapping MI.

2. Furthermore, the followed field verification work discovered two Pb–Zn mineralization zones and proved our remote sensing study is effective in the region.
3. Concerning about the abundant cerusite, smithsonite, and gypsum discriminated in the mineralization zones, we describe the Huoshaoyun Pb–Zn ore as the MVT-SOT.
4. The results of the study show that Landsat 8 OLI and ASTER data accompanied with series of image processing techniques have provided a simple, robust, and economical approach for exploration geologists to detect carbonate mineral indicators associated with lead–zinc ore and related host rock. Due to the extensively distributed stratums and structures along the west Kunlun belt, the ore prospecting methodology could be applied in similar geological settings, especially in inaccessible, high-elevation areas with low vegetation coverage.

Acknowledgments

This research was supported by the National Nature Science Foundation of China (Vote no: 41502312), Chinese Ministry of Science and Technology (Vote no: 2015BAB05B03-01), and China Geological Survey Foundation (Vote no: DD20160002, DD20160336).

References

1. L. C. Rowan et al., "Discrimination of rock types and detection of hydrothermally altered areas in south-central Nevada by the use of computer-enhanced ERTS images," *Geol. Surv. Prof. Paper* **35**, 1–35 (1974).
2. A. F. H. Goetz, B. N. Rock, and L. C. Rowan, "Remote sensing for exploration: an overview," *Econ. Geol.* **78**, 573–590 (1983).
3. M. J. Abrams et al., "Remote sensing of porphyry copper deposits in southern Arizona," *Econ. Geol.* **78**, 591–604 (1983).
4. L. C. Rowan, A. F. H. Goetz, and R. P. Ashley, "Discrimination of hydrothermally altered and unaltered rocks in visible and near-infrared multispectral images," *Geophysics* **42**, 522–535 (1977).
5. X. Zhang, M. Pazner, and N. Duke, "Lithological and mineral information extraction for gold exploration using ASTER data in the south Chocolate Mountains, California," *ISPRS J. Photogramm. Remote Sens.* **62**, 271–282 (2007).
6. S. M. Hassan and T. M. Ramadan, "Mapping of the late Neoproterozoic Basement rocks and detection of the gold-bearing alteration zones at Abu Marawat-Semna area, Eastern Desert, Egypt using remote sensing data," *Arabian J. Geosci.* **8**, 4641–4656 (2015).
7. A. B. Pour and M. Hashim, "Hydrothermal alteration mapping from Landsat 8 data, Sar Cheshmeh copper mining district, south-eastern Islamic Republic of Iran," *J. Taibah Univ. Sci.* **42**, 1309–1323 (2015).
8. US Geological Survey, *Landsat Data Continuity Mission*, U.S. Geological Survey, Washington, DC (2012).
9. I. Di Tommaso and N. Rubinstein, "Hydrothermal alteration mapping using ASTER data in the Infiernillo porphyry deposit, Argentina," *Ore Geol. Rev.* **32**, 275–290 (2007).
10. Z. Adiri et al., "Lithological mapping using Landsat 8 OLI and Terra ASTER multispectral data in the Bas Draa inlier, Moroccan Anti Atlas," *J. Appl. Remote Sens.* **10**, 016005 (2016).
11. M. Pournamdari and M. Hashim, "Detection of chromite bearing mineralized zones in Abdasht ophiolite complex using ASTER and ETM+ remote sensing data," *Arabian J. Geosci.* **4**, 1–11 (2013).
12. G. R. Hunt, "Spectral signatures of particulate minerals in the visible and near infrared," *Geophysics* **42**, 501–513 (1977).

13. M. Abrams, "Distribution of subsurface hydrocarbon seepage in near-surface marine sediments," in *Hydrocarbon Migration and Near Surface Expression*, D. Schumacher and M. A. Abrams, Eds., Vol. **66**, pp. 1–14, AAPG, Houston, Texas (1996).
14. Z. Zhang et al., "Iron and sulfur speciation in some sedimentary-transformation type of lead-zinc deposits in West Kunlun lead-zinc ore deposit zone, Northwest China," *J. Radioanal. Nucl. Chem.* **297**, 83–90 (2013).
15. Z. Zhang, J. Peng, and J. Xiao, "Regional metallotectonics of the lead-zinc deposits zone in southwest margin of the Tarim plate," *Bull. Miner. Petrol Geochem.* **28**, 318–329 (2009).
16. Y. Dong, K. Guo, and H. Xiao, "Ore forming conditions and prospecting in the west Kunlun area, Xinjiang, China," *Acta Geol. Sin.* **78**, 345–351 (2004).
17. Q. Jia, *Massive Sulfide Copper Deposits of West Kunlun, Xinjiang*, Geological Publishing House, Beijing, China (1999).
18. Y. Dong, K. Guo, and S. Liao, "Geological and geochemical characteristics of the Keluxilik lead-zinc ore deposit, west Xinjiang," *Acta Geol. Sin.* **88**, 1730–1738 (2006).
19. Z. Zhang, J. Peng, and J. Xiao, "Regional metallotectonics of the lead-zinc deposits zone in southwestern margin of the Tarim plate," *Bull. Miner. Petrol. Geochem.* **28**, 42–43 (2010).
20. H. Guo et al., "Use of multifrequency, multipolarization shuttle imaging radar for volcano mapping in the Kunlun Mountains of western China," *Remote Sens. Environ.* **59**, 364–374 (1997).
21. A. Lin and J. Guo, "Nonuniform slip rate and millennial recurrence interval of large earthquakes along the eastern segment of the Kunlun Fault, northern Tibet," *Bull. Seismol. Soc. Am.* **98**(6), 2866–2878 (2008).
22. W. Jia et al., "The application of remote sensing and aero-geophysics data fusion on metallogenic prognosis in qimantage of East Kunlun Mountain area," in *Paper Presented at the 3rd ISPRS Int. Archives of the Photogrammetry, Remote Sensing and Spatial Information Sciences*, Vol. XL-7/W1, pp. 49–53 (2013).
23. Z. He, B. He, and Y. Cui, "Hydrothermal alteration mapping using ASTER data in East Kunlun Mountains, China," in *Paper Presented at the IEEE Int. Geoscience & Remote Sensing Symp. (IGARSS 2010)*, Honolulu, Hawaii, USA, pp. 4514–4517, IEEE (2010).
24. B. Fu and A. Lin, "Spatial distribution of the surface rupture zone associated with the 2001 Ms 8.1 Central Kunlun earthquake, northern Tibet, revealed by satellite remote sensing data," *Int. J. Remote Sens.* **24**(24), 2191–2198 (2003).
25. L. Liu et al., "Gold-copper deposits in Wushitala, Southern Tianshan, Northwest China: application of ASTER data for mineral exploration," *Geol. J.* **3**, 1–10 (2017).
26. L. Liu et al., "Mineral mapping and ore prospecting using Landsat TM and Hyperion data, Wushitala, Xinjiang, northwestern China," *Ore Geol. Rev.* **81**, 280–295 (2017).
27. X. Wang, Z. Xie, and Y. Wu, "Study on information extraction of remote sensing mineralizing alteration anomaly in Tashkuergan area of West Kunlun Mountain," *Contrib. Geol. Miner. Res. Res. Chin. Ed.* **2**, 136–139 (2002).
28. X. Wang et al., "Discussion on application of WorldView 2 satellite data in West Kunlun metallogenic belt remote sensing geological survey," *Proc. SPIE* **9158**, 91580I (2014).
29. M. Yang et al., "Uses of WorldView-2 multispectral data in extracting potential iron mineralization zones," *Adv. Eng. Res.* **12**, 1860–1868 (2015).
30. F. F. Sabins, "Remote sensing strategies for mineral exploration," *Ore Geol. Rev.* **14**, 157–183 (1999).
31. Y. Ninomiya, "Stabilized vegetation index and several mineralogic indices defined for ASTER VNIR and SWIR data," *IEEE. Int. Geosci. Remote Sens. Symp.* **3**, 1552–1554 (2003).
32. J. C. Mars and L. C. Rowan, "Spectral assessment of new ASTER SWIR surface reflectance data products for spectroscopic mapping of rocks and minerals," *Remote Sens. Environ.* **114**, 2011–2025 (2010).
33. S. Gabr, A. Ghulam, and T. Kusky, "Detecting areas of high-potential gold mineralization using ASTER data," *Ore Geol. Rev.* **38**, 59–69 (2010).
34. J. R. Harris et al., "Mapping lithology in Canada's Arctic: application of hyperspectral data using the minimum noise fraction transformation and matched filtering," *Can. J. Earth Sci.* **42**, 2173–2193 (2005).

35. L. Dong et al., "Discovery of the Huoshaoyun super-large exhalative sedimentary carbonate Pb-Zn deposit in the western Kunlun area and its great significance for regional metallogeny," *Xinjiang Geol.* **33**, 41–50 (2015).
36. A. B. Pour and M. Hashim, "Identifying areas of high economic-potential copper mineralization using ASTER data in the Urumieh-Dokhtar Volcanic Belt, Iran," *Adv. Space Res.* **49**, 753–769 (2012).
37. E. Bedini, "Mineral mapping in the Kap Simpson complex, central East Greenland, using HyMap and ASTER remote sensing data," *Adv. Space Res.* **47**, 60–73 (2011).
38. L. Liu et al., "The reconnaissance of mineral resources through ASTER data-based image processing, interpreting and ground inspection in the Jiafushaersu Area, West Junggar, China," *J. Earth Sci.* **25**, 397–406 (2014).
39. D. W. Leverington and W. M. Moon, "Landsat-TM-based discrimination of lithological units associated with the Purtuniq ophiolite, Quebec, Canada," *Remote Sens.* **4**, 1208–1231 (2012).
40. L. Yu et al., "Towards automatic lithological classification from remote sensing data using support vector machines," *Comput. Geosci.* **45**, 229–239 (2012).
41. N. Li, "Textural and rule-based lithological classification of remote sensing data, and geological mapping in Southwestern Prieska sub-basin, Transvaal Supergroup, South Africa," PhD Thesis, University of Munich, Germany (2010).
42. A. B. Pour and M. Hashim, "Identification of hydrothermal alteration minerals for exploring of porphyry copper deposit using ASTER data, SE Iran," *J. Asian Earth Sci.* **42**, 1309–1323 (2011).
43. R. Amer, T. Kusky, and A. E. Mezayen, "Remote sensing detection of gold related alteration zones in Um Rus area, Central Eastern Desert of Egypt," *Adv. Space Res.* **49**, 121–134 (2012).
44. A. Moghtaderi, F. Moore, and A. Mohammadzadeh, "The application of advanced spaceborne thermal emission and reflection (ASTER) radiometer data in the detection of alteration in the Chadormalu paleocrater, Bafq region, Central Iran," *J. Asian Earth Sci.* **30**, 238–252 (2007).
45. R. Amer, T. Kusky, and A. Ghulam, "Lithological mapping in the Central Eastern Desert of Egypt using ASTER data," *J. Afr. Earth Sci.* **56**, 75–82 (2010).
46. O. Crouvi et al., "Quantitative mapping of arid alluvial fan surfaces using field spectrometer and hyperspectral remote sensing," *Remote Sens. Environ.* **104**, 103–117 (2006).
47. Y. Xiong et al., "Lithological mapping of Bela ophiolite with remote-sensing data," *Int. J. Remote Sens.* **32**, 4641–4658 (2011).
48. S. M. Hassan and M. F. Sadek, "Geological mapping and spectral based classification of basement rocks using remote sensing data analysis: the Korbiai-Gerf nappe complex, South Eastern Desert, Egypt," *J. Afr. Earth Sci.* **134**, 404–418 (2017).
49. M. W. Mwaniki, M. S. Moellen, and G. Schellmann, "A comparison of Landsat 8 (OLI) and Landsat 7 (ETM+) in mapping geology and visualizing lineaments: a case study of central region Kennya," in *Paper Presented at the 36th ISPRS Int. Archives of the Photogrammetry, Remote Sensing and Spatial Information Sciences*, Vol. Xl-7/W3, pp. 897–903 (2015).
50. S. Behnam et al., "Using ETM+ and ASTER sensors to identify iron occurrences in the Esfordi 1:100, 000 mapping sheet of Central Iran," *J. Afr. Earth Sci.* **85**, 103–114 (2013).
51. Y. Liu et al., "Hydrothermal fluid origins of carbonate-hosted Pb-Zn deposits of the Sanjiang Thrust Belt, Tibet: indications from noble gases and halogens," *Econ. Geol.* **112**, 1247–1268 (2017).
52. Y. Wang et al., "Palaeogene sediment-hosted Pb-Zn deposits in SE Asia: the Uragen example," *Int. Geol. Rev.* **59**, 1–15 (2017).
53. J. C. Mars and L. C. Rowan, "Regional mapping of phyllic-and argillicaltered rocks in the Zagros magmatic arc, Iran, using Advanced Spaceborne Thermal Emission and Reflection Radiometer (ASTER) data and logical operator algorithms," *Geosphere* **2**, 161–186 (2006).
54. F. J. Kruse and S. L. Perry, "Mineral mapping using simulated WorldView-3 short-wave-infrared imagery," *Remote Sens.* **5**, 2688–2703 (2013).

55. F. J. Kruse, W. M. Baugh, and S. L. Perry, "Validation of DigitalGlobe WorldView-3 Earth imaging satellite shortwave infrared bands for mineral mapping," *J. Appl. Remote Sens.* **9**, 096044 (2015).
56. B. Ye et al., "Assessment of WorldView-3 data for lithological mapping," *Remote Sens.* **9**, 1132–1150 (2017).

Min Yang is an assistant researcher at the Key Laboratory for the Magmatism and Giant Ore Deposits, Ministry of Land and Resources. He received his BS and MS degrees in geoinformation and remote sensing from the Chang'an University in 2007 and 2010, respectively. He is pursuing his on-the-job Dr. Degree in Chang'an University. His current research interests include mineral mapping using remotely sensed data and geoinformation system, near-infrared spectroscopy of minerals.

Guangli Ren is an assistant researcher at the Key Laboratory for the Magmatism and Giant Ore Deposits, Ministry of Land and Resources. He received his BS degree in geosciences from Xinjiang University in 2006. He received his Dr. degree in ore geology from Guangzhou Institute of Geochemistry, Chinese Academy of Sciences. His current research interest is ore geology survey.

Ling Han is a professor of Chang'an University. She received her Dr. degree in geoinformation from the Northwestern University, Xi'an, China, in 2005. Her current research interest is geoinformation and geological application.

Huan Yi is a assistant researcher in Xi'an Center of China Geological Survey. She received her BS and MS degrees in geoinformation from China University of Geosciences in 2006 and 2009, respectively. Her current research interests include geoinformation system and remote sensing application.

Ting Gao is a assistant researcher in Xi'an Center of China Geological Survey. She received her BS and MS degrees in geoinformation from China University of Geosciences in 2004 and 2011, respectively. Her current research interests include ore geological survey and remote sensing application.